Biomedical Optics EXPRESS

High-throughput 3D imaging of single cells with light-sheet fluorescence microscopy on chip

FEDERICO SALA,[1,2] MICHELE CASTRIOTTA,[1,2] PETRA PAIÈ,[2] ANDREA FARINA,[2] SARAH D'ANNUNZIO,[3] ALESSIO ZIPPO,[3] ROBERTO OSELLAME,[1,2] FRANCESCA BRAGHERI,[2,*] AND ANDREA BASSI[1,2]

[1] *Department of Physics, Politecnico di Milano, Piazza Leonardo da Vinci 32, 20133 Milano, Italy*
[2] *Istituto di Fotonica e Nanotecnologie, CNR, Piazza Leonardo da Vinci 32, 20133 Milano, Italy*
[3] *Laboratory of Chromatin Biology & Epigenetics, Center for Integrative Biology (CIBIO), University of Trento, 38123, Trento, Italy*
[*] *francesca.bragheri@ifn.cnr.it*

Abstract: Single-cell analysis techniques are fundamental to study the heterogeneity of cellular populations, which is the basis to understand several biomedical mechanisms. Light-sheet fluorescence microscopy is a powerful technique for obtaining high-resolution imaging of individual cells, but the complexity of the setup and the sample mounting procedures limit its overall throughput. In our work, we present an optofluidic microscope-on-chip with integrated microlenses for light-sheet shaping and with a fluidic microchannel that allows the automatic and continuous delivery of samples of a few tens of microns in size. The device is used to perform dual-color fluorescence analysis and 3D reconstruction of xenograft-derived mouse breast cancer cells.

1. Introduction

Light Sheet Fluorescence Microscopy (LSFM) experienced a significant development in the last years. Starting from the first setup proposed by Huisken et al. [1], several illumination and detection geometries [2] have been adopted and, subsequently, different advanced techniques like two-photon microscopy [3] or structured illumination microscopy [4] have been integrated in the same setup.

LSFM is used in biological studies because of its low photobleaching, fast image acquisition and intrinsic 3D reconstruction capabilities. It allows the acquisition of different samples of different sizes, ranging from single cells and spheroids [5] to millimeter sized specimens, like Drosophilas or zebrafish embryos [1] and plants [6].

Similarly to many single cell analysis techniques [7], standard LSFM implementations are limited by a low throughput: the time required to prepare the sample, along with the alignment procedure, limits the effective number of samples that can be analysed. However, the possibility to investigate a large number of samples at single cell resolution has a great value for many biological applications, since it allows statistical analysis of heterogeneous or nominally homogeneous populations. Indeed the study of a population as a whole is intrinsically based on average measurements and this could mask specific characteristics of minority sub-populations [8].

A solution to these problems comes from microfluidics [9]. Instead of translating the light-sheet through the sample, the cells are flown in a microchannel passing through a prealigned illumination stage, allowing a precise and continuous scanning. A first demonstration of this approach has been realized combining a PDMS microchannel with LSFM realizing a light-sheet based fluorescence cytometer [10] applicable to study either single cells [11], phytoplankton [12] or zebrafish embryos [13]. Microfluidics has already been used to achieve high-throughput

#393892
Journal © 2020
https://doi.org/10.1364/BOE.393892
Received 30 Mar 2020; revised 1 Jun 2020; accepted 2 Jun 2020; published 17 Jul 2020

in fluorescence cytofluorimetric applications, as standard FACS or in more advanced imaging techniques [14]. A further step has been the integration of optical elements on the microfluidic platform itself, like 45° mirrors, in order to reduce the complexity of the light-sheet generation setup. This approach has been used both with microchannels [15,16] and microreservoirs arrays [17].

In our previous work [18], we proposed to increase the level of integration by embedding both the microfluidic network and illumination micro-optics in a single compact device. In this way the light, coming from a prealigned optical fiber, passes through a fixed cylindrical lens realized in the same substrate of the microchannel, without the need for further operator. The chip is placed in a conventional wide-field microscope, and it provides both light-sheet illumination and sample scanning, i.e. the sample automatically flows through the light-sheet. This microscope-on-chip was designed for the analysis of biological samples with dimensions of hundreds of micrometers, which includes spheroids, organoids or small embryos. The technique used to realize this device is called Femtosecond Laser Micromachining Followed by Chemical Etching (FLICE) [19]. It allows the realization of both optical and microfluidic components with arbitrary 3D geometry during the same fabrication step and on the same glass substrate.

In this work, we present the realization of a new chip tailored for high-throughput single cell imaging, fabricated with FLICE. We present its design and optimization and we discuss the challenges linked to the small dimensions of the sample (cell size around 15 μm) and the technological solutions required to achieve automatic, high resolution imaging of cells flowing in the optofluidic device. In particular we describe: (i) the design of a chip compatible with high numerical aperture objective lenses; (ii) the design and the fabrication of the microchannel for automatic and controlled flow of single cells; (iii) the optical design and the optimization needed for the development of dual-color light-sheet illumination, which is required in the majority of cell biology applications.

Our aim is to realize a device that could achieve high-resolution imaging, being at the same time compact, user friendly, potentially low cost, and compatible with a wide-field microscope.

2. Chip design and fabrication

We designed an optofluidic chip that could be mounted on a standard inverted microscope, as a functional add-on. The chip includes a three dimensional fluidic network, through which the cells are flown, and the illumination path for light-sheet microscopy: an optical fiber illuminates a hollow cylindrical lens (see Section 2.3) to create a light sheet in a single plane crossing the channel. The microfluidic network is a single U shaped microchannel with a detection window at the bottom, as described in detail in Section 2.2. The excitation lasers are coupled to the device with a single mode optical fiber, in order to be directly connectable to standard pigtailed lasers sources and to avoid the need of external coupling stages. The optical fiber is glued to the device and its alignment is guaranteed by a O-groove, realized with the same process of the channel and the lens [20]. The whole device has a footprint of $6x3x2\ mm^3$ and it can be mounted on a custom sample holder with the same dimensions of a microscope glass slide, maintaining the alignment with the external movement stages of the wide-field microscope. In Fig. 1 a picture of the final device is shown, along with the scheme of the internal geometry.

2.1. Micromachining technique: FLICE

The choice of this microfabrication technique is important because of its high 3D design freedom. Indeed, LSFM detection-excitation orthogonal geometry implies the realization of elements along all 3 spatial directions. Furthermore, the possibility to realize all the elements in a single irradiation step and on the same substrate guarantees their perfect alignment already at the fabrication stage. The use of an inert glass material is naturally compatible with any biological sample or drug, and, because of its optical characteristics, it is ideal for the realization of refractive

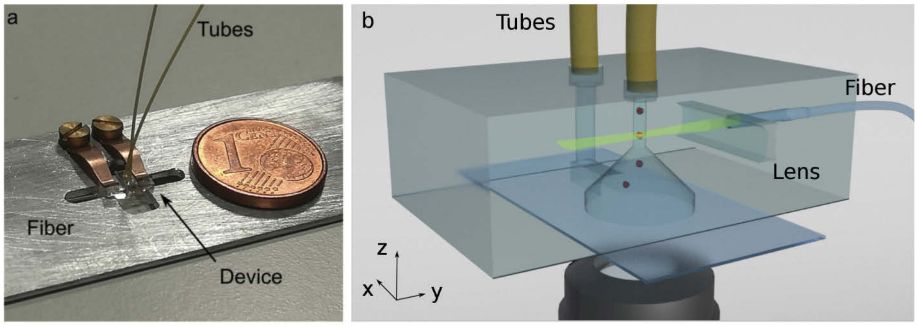

Fig. 1. (a) Picture of the device mounted on the custom holder (in comparison with a 1 € cent coin) (b) Complete device representation, not to scale.

elements like lenses. Lastly, this technique easily allows the modification of the final device geometry by changing the laser irradiation path, thus it allows fast and cost-effective prototyping.

2.2. Microchannel

Microfluidics is used for precise and continuous sample delivery. In our device a single U shaped microchannel is present, with one inlet and one outlet connected to the sample vial and to the external pumping system by biocompatible polyether ether ketone (PEEK) tubes, with internal diameter of 100 μm and length of $\approx$ 15 cm. The detailed design is shown in Fig. 2.

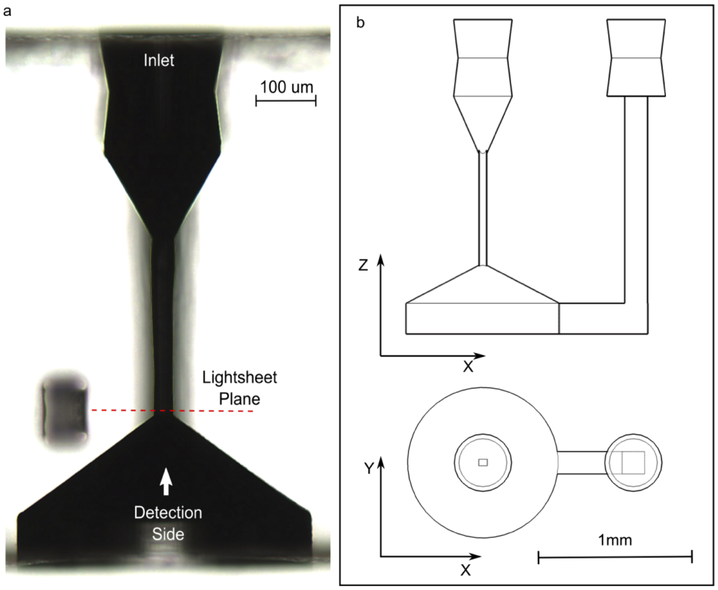

Fig. 2. (a) Microscope image of the detection channel before device assembling, yz view. (b) Orthogonal views of microchannel.

As sample target, we considered cells with a diameter spanning from 15 μm to 25 μm. Therefore, as a consequence we designed and fabricated the first part of the microchannel with a cross section of 80 μm $\times$ 50 μm, along x and y direction respectively, so that only few cells could pass simultaneously. This small cross section fits well with the field of view of an high numerical aperture, high magnification objective. Such capillary is joined to the tube connection with a tapered inlet, as shown in panel (a) of Fig. 2.

Focusing deep inside a small channel buried in glass could give problems from the imaging point of view. Specifically, the refractive index mismatch between the device substrate (fused silica), the surrounding media (air) and the sample buffer (aqueous solution) could induce aberrations and consequently degrade the image resolution. As first solution we decided to use a water immersion objective (60x 1.1 NA), with a correction collar for thin glass coverslips and then we designed the microchannel to avoid refraction of light at the chip edges. We realized an open channel and sealed it afterwards with an optical quality coverslip. The sealing was performed with a UV curable glue (DELO photobond GB345), taking advantage of capillary forces to distribute the glue uniformly, without invading in the open channel. Moreover we tapered the channel itself, in order to avoid aberrations induced by the transparent lateral walls, by introducing a conical funnel with a 56° angle and a base diameter of $\approx 1\ mm$, obtained taking into consideration the projection of the cone defined by the numerical aperture of the detection objective. The effects of this shape on the sample trajectory has been studied in detail, as reported in Section 3.4.

2.3. Hollow microlens

The design of the optical elements has been first studied via software simulation using *OpticStudio Zemax*. Several lenses have been then realized to calibrate the fabrication process, comparing simulations and experimental results. Once separately optimized, the optical elements have been directly integrated in the final device, with minor changes needed.

The requirements of the light-sheet are the following: FWHM of $2\ \mu m$, and dimension along the other two directions larger than $50\ \mu m$ to cover the whole detection area, negligible chromatic aberrations, simplicity in realization and assembling. Because of the last two points, we decided to realize a hollow embedded cylindrical microlens, by fabricating a microchannel with engineered cross section able to focus the light coming from an optical fiber thanks to the refractive index mismatch between the substrate (Fused Silica $n \approx 1.46$) and air ($n = 1$). Specific constraints are: (i) the lens thickness, fixed to $\approx 60\ \mu m$ by the fabrication process, (ii) its maximum semiaperture of $290\ \mu m$, limited by the free spaces adjacent to the microchannel, and (iii) the optical fiber mode dimension and NA (Thorlabs SM450 single mode optical fiber, $4.1\ \mu m$ mode dimension, 0.14 NA at 488 nm). We initially designed a cylindrical biconcave hollow lens and optimized its radii of curvature, aperture and position firstly by geometrical optics and then by physical optics simulations. In the final design, the biconcave lens presented radii of curvature of $160\ \mu m$ and $98\ \mu m$, a semi-aperture of $60\ \mu m$, an equivalent NA of 0.31 and a simulated light-sheet spot-size of $\approx 8.6\ \mu m$. Ray tracing simulation predicted a marginal ray impinging angle of 18.5°. Under this condition, spherical aberrations strongly affect the microlens performances. We therefore realized a second design consisting in a cylindrical hollow microlens with two aspherical surfaces. The ray tracing simulation for this lens is reported in Fig. 3, while the complete parameters are reported in Data File 1. This new design guarantees a light-sheet of $1.6\ \mu m$ and $1.7\ \mu m$ FWHM for 488 nm and 561 nm illumination wavelength, respectively. At the same time the lens guarantees an almost uniform thickness of the light-sheet along its propagation axis, with a FWHM of $3.2\ \mu m$ for both 488 nm and 561 nm measured at the edge of the FOV, i.e at $5\ \mu m$ from the channel walls. Chromatic aberrations induce a focal shift of $3.1\ \mu m$ between the two light-sheets generated at different wavelength, which is negligible if compared to the detection channel size. We repeated the simulations using an index-matching solution inside the microchannel and the results showed variation in the thickness, computed in different positions, lower than 5% from the previous case, which can be therefore considered negligible.

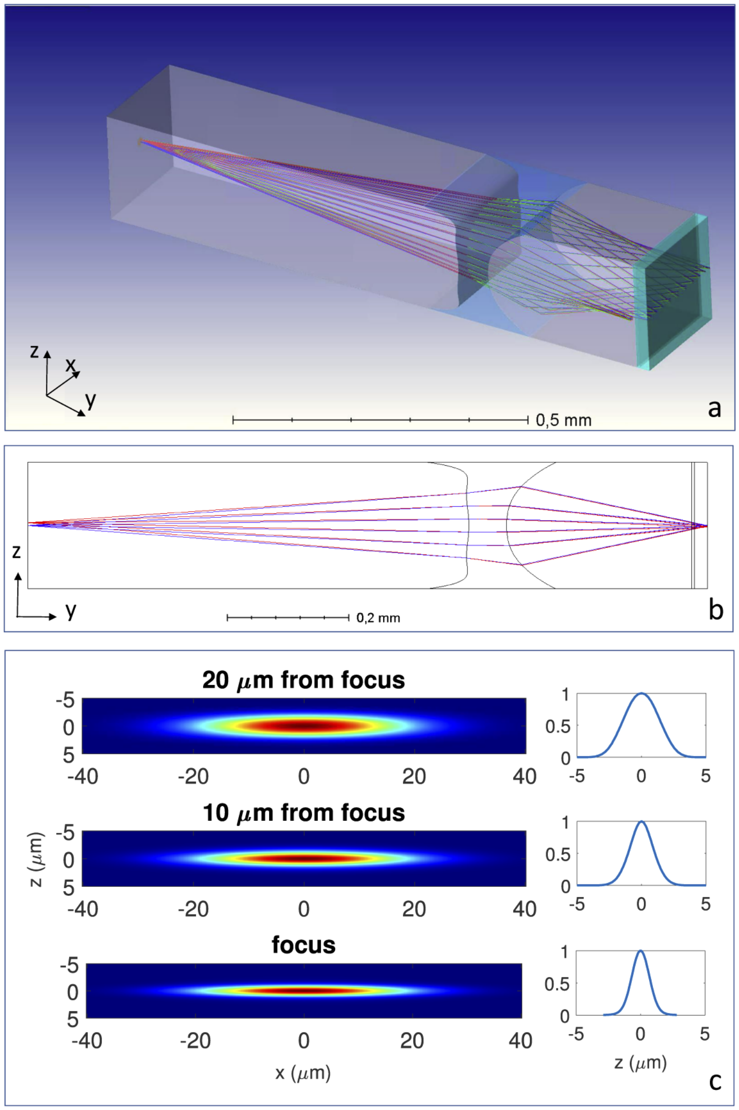

Fig. 3. Zemax simulation of the aspheric profile hollow microlens for 488 nm wavelength. (a) 3D model of the optical system with ray tracing of the 3 point-like sources used for initial optimization. (b) Lateral view of ray tracing simulation. (c) Physical optics simulation of the xz normalized intensity profile at lens focal plane, 10 μm and 20 μm before the focus. For each xz plot the corresponding profile at x=0 is reported on the right hand side.

We performed a scan on the simulated parameters to study the robustness against fabrication defects and we found that small changes of the first order radius of curvature of both spheric and aspheric surface could degrade the performances of the lenses. Thus an accurate calibration of the fabrication process was required, as described in Section 3.3

3. Experimental validation

3.1. Experimental setup

The device has been designed in order to be easily integrated on an existing inverted microscope setup. For this reason we designed a custom chip-holder consisting of an aluminium plate with the same dimensions of a conventional microscope slide, clamps to fix the device and a slot to allow imaging from below. The holder was mounted on an experimental setup working as a typical inverted fluorescence microscope.

We used two Coherent OBIS lasers with 561 *nm* and 488 *nm* emission wavelengths as excitation light sources. The two lasers are firstly coupled to two different optical fibers, and then combined in a single fiber with a commercial wavelength combiner (Thorlabs GB19A1). Considering a typical cell size of 15 μm in diameter, the cells speed was set to a value in the range 15 $\mu m/s$ – 150 $\mu m/s$. The detection arm is composed by a 60x, 1.1 NA water immersion objective (Olympus LUMFLN60XW) with correction ring, Olympus U-TV1XC tube lens and Hamamatsu Orca Flash 4.0 V3 detection camera. This camera is a 2048 × 2048 pixel CMOS camera with a maximum frame rate of about 100 *Hz*, but in our application we reduced the active area to 700 × 500 pixel increasing the acquisition frequency up to 400 *Hz*. This corresponds to a FOV of 76 μm *by* 54 μm. We used a dual band filter (Semrock FF01-512/630-25) to detect the fluorescence of two different markers with a single detector. For the microfluidic control, we used two 25 *mbar* channels of a Fluigent MAESFLOW pressure-based fluidic pump. All hardware components were controlled by a single Python custom-made program based on ScopeFoundry (http://www.scopefoundry.org/) [21] open source software.

We performed the dual color acquisition in a sequential mode, i.e. shining the sample alternatively with the two lasers. The lasers and the camera are triggered with two external signals generated by a DAQ board (National Instrument NI USB-6212) combined with a custom logical port. In order to increase the maximum frame rate of the detection camera, we used a rolling shutter mode. In this mode, the pixel lines of the CMOS detector are read-out sequentially and at the same time the emptied lines could start the next frame acquisition. This implies that the central part of the sensor will start to acquire the following frame (i.e. the following color channel) earlier than the external one, generating a cross talk between the two excitation wavelengths. To overcome this issue we used the DAQ signals to trigger the lasers in order to switch them off during the sequential readout time interval and to switch them on only when the whole sensor is active, ensuring that each frame is illuminated by one laser per time.

3.2. Sample preparation protocols

The cells used in this study are hTERT-immortalized human mammary epithelial cells (WT IMEC) and xenograft-derived primary tumor cells (XDs), previously used in [22]. Both cell lines are transduced with PGK-H2B mCherry lentiviral vector and immunolabeled with Alexa488 targeted to alpha-tubulin. For the immunofluorescence procedure, 1 million cells were fixed in 4%PFA for 10 minutes and then were processed in suspension as follow: permeabilization and blocking with PBS/1% BSA/5% goat serum/0.5% Triton X-100 (blocking solution-BS) for 1 hour at room temperature- RT, incubation with primary antibody diluted in the BS for 2 hours at RT, 3 washes in PBS, incubation with secondary antibodies (diluted in the BS) and other 3 washes in PBS.

In order to avoid cell aggregation and possible clogging of the microfluidic system, ethylenediamine tetraacetic acid (EDTA) at 5 *mmol* concentration is added to the sample. The sample volume uploaded in the system is 0.5 *ml* at a concentration of 1 $million\ cell/ml$ in PBS buffer solution. It is also possible to increase the liquid viscosity using as buffer an index matching agent 2,2-thiodiethanol (TDE), in a ratio of 2:3, in order to match the surrounding glass refractive index.

3.3. Light-sheet generation analysis

Once the optimal aspheric lens profile is obtained from simulation, it was replicated directly in the substrate by laser irradiation, with the precision guaranteed by the fabrication setup. However, the second step of FLICE process, i.e. the HF etching, could introduce some minor deformations because of the limited selectivity of the etching process. Consequently a calibration of the laser writing process is needed. We developed a simple correction algorithm to define the laser irradiation pattern able to generate the desired lens profile after etching. This algorithm considers the fused silica surface to be etched by hydrofluoric acid solution along its normal direction at the fixed etching rate of the pristine material [23]. By back projecting the desired surface by the time required to develop the whole structure, it has been possible to define the compensated irradiation geometry. The profile of etched lenses observed at optical microscope confirmed the effectiveness of the correction. An example of the difference between the irradiated profile and etched one is reported in Fig. 4.

Afterwards, we realized several hollow lenses in order to test the correction parameters and compare the experimental results against the simulated performances, by slightly adjusting position, thickness and radii of irradiated structures. We realized a reservoir to be filled with rhodamine solution in front of the lens, in the same position of the microchannel in the final design.

We characterized the thickness of the generated light-sheet by imaging the fluorescence signal of the rhodamine from the side. The same experimental approach has been used to characterize the light-sheet of the complete device. In Fig. 4 the fluorescence profile of the rhodamine inside the inlet channel is shown, along with the fit of the acquired data. More details on the experimental measurement are reported in [18,24].

From our measurements we were able to obtain a minimum FWHM thickness of 4.88 μm for spherical lenses and 2.10 μm for the aspherical ones, measured at 532 *nm* of excitation wavelength. The discrepancy between the theoretical value and the measured one could be mainly imputed to some minor deviations of the lens profile from the theoretical one and to the presence of residual roughness due to the etching process.

We integrated the lens with the microfluidic channel and we acquired several stacks of flowing fluorescent nanobeads with a diameter of $\approx$ 100 *nm*, emitting at 650 *nm*, suspended in index matched solution. From this analysis we obtained a lateral FWHM of the PSF of 0.51 μm, bigger than theoretical diffraction limit of $d = \lambda/(2 * NA) = 0.295\ \mu m$. This could be due to the residual spherical aberrations introduced by the microchannel. A second contribution could come from movement of the nanobeads during the acquisition, because of their the brownian motion in the liquid buffer. We tracked the average motion of the nanobeads during the acquisition and we estimated a motion blur in the order of 250 *nm*, comparable with our lateral PSF broadening. The same effect will not be as relevant when dealing with bigger samples, like single cells.

3.4. Sample trajectory analysis

Three dimensional reconstruction in LSFM is obtained by acquiring several planes one after the other and stacking them together afterwards. During this operation we implicitly convert a temporal stack into a spatial one, assuming that the translation axis of either the sample or of the light-sheet remains constant during the whole process. Even though some strategies have been

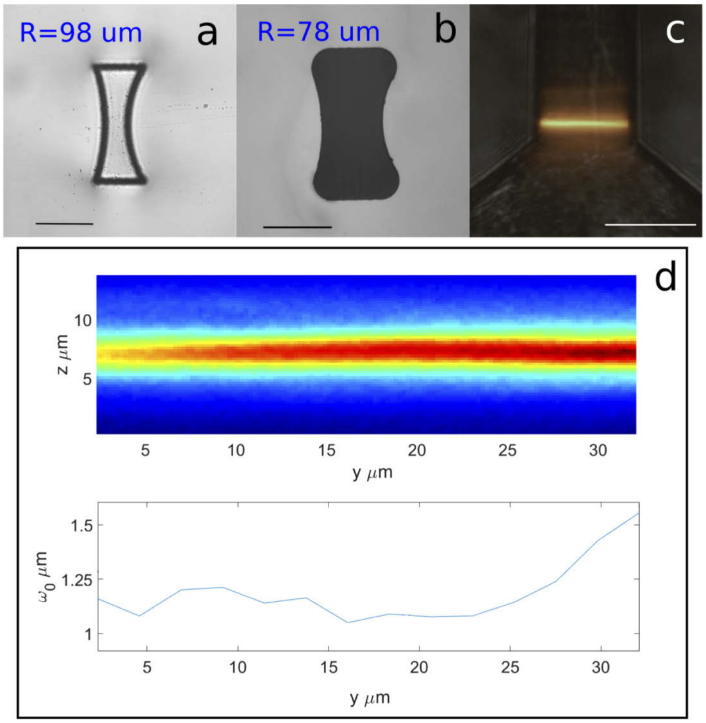

Fig. 4. Example of spheric cylindrical microlens with 78 μm curvature radius of right hand surface. Microscope images before (a) and after etching (b). The radius of each lens is reported. It can be seen that the precompensation of the irradiated geometry leads to the correct final dimension; (c) Image of the rhodamine signal, inside the inlet microchannel, when irradiated by the light-sheet. Superposition of fluorescence and bright-field channels; All scalebars correspond to 50 μm. (d) Acquired image of light-sheet fluorescence profile and corresponding waist fit ($\omega_{min} = FWHM/2 = 1.05$ μm). The plot shows the fit of the light sheet waist taking into consideration the acquisition objective depth of field. Each point is averaged on 10 raw data points. This plot corresponds to half of the light-sheet thickness.

developed to compensate possible shifts of the sample, like the use of nanobeads embedded in the sample holder media as reference position marks, these are not suitable for our device, that make use of buffer flow to move the sample.

We simulated and tested experimentally the trajectory of cell-like bodies in our detection channel to see whether its widening cross section could introduce relevant perturbations in the laminar flow. We realized ad hoc prototypes to track the trajectory of polystyrene microbeads (16 μm diameter) throughout the whole channel. The trajectory of the beads along the channel results to be straight and parallel to the z axis. Some deviations from this trajectory are introduced slightly before the channel widening. We then decided to place the light-sheet 10 μm before the beginning of the conical section of the channel. We focused our attention on the shift of their lateral position while passing through the plane of the light-sheet. We estimated an average lateral shift of 0.15 μm over a total axial displacement of 25 μm, much smaller than the typical size of our target samples, which could be anyway compensated with standard registration algorithms.

4. Dual color single cell acquisition

Once we characterized the performances of the system, we proceeded with the device validation with biological samples. We used human mammary epithelial cells, both WT IMEC and XD lines described in Section 3.2. The cells have a diameter of approximately 15 μm, totally compatible with our device, and we performed several measurements acquiring from 10 to 200 planes per cell by adjusting the pressure at the inlet.

The maximum acquisition frame rate corresponds to 400 Hz. The camera shutter has been synchronized with the laser switch control, to precisely illuminate the sample with one laser only at a time in an alternate fashion, reaching a maximum single channel frame rate of 200 Hz.

The cells concentration in the liquid is 1M/ml, similar to the one used in flow cytometry applications, which gives an acquisition throughput of approximately 1 $sample/s$, as is shown in the Visualization 1. At this flux rate, the sample is scanned at approximately 150 $\mu m/s$ and the images are acquired at 100 Hz frame rate per channel. This corresponds to the acquisition of an average of 10 sections per cell for each color channel, with steps of $1 - 1.5$ μm. In order to further increase the throughput, one strategy could be to locally increase the concentration of cells in the chip, for example with the integration of flux focusing techniques [25].

In order to obtain finer sampling, the speed can be reduced. An example of acquisition at lower speed is shown in Fig. 5: the axial scanning is 0.1um and 100 sections per sample (per channel) are acquired in 1 s acquisition. Here the speed was set at 15 $\mu m/s$, which corresponds to flow rate of 0.0036 $\mu l/min$. Such a low flow regime was achieved working at the minimum pressure step guaranteed by the pump system (0.025 $mbar$) and adjusting the connection tubes length, in order to increase the overall fluidic resistance of the device.

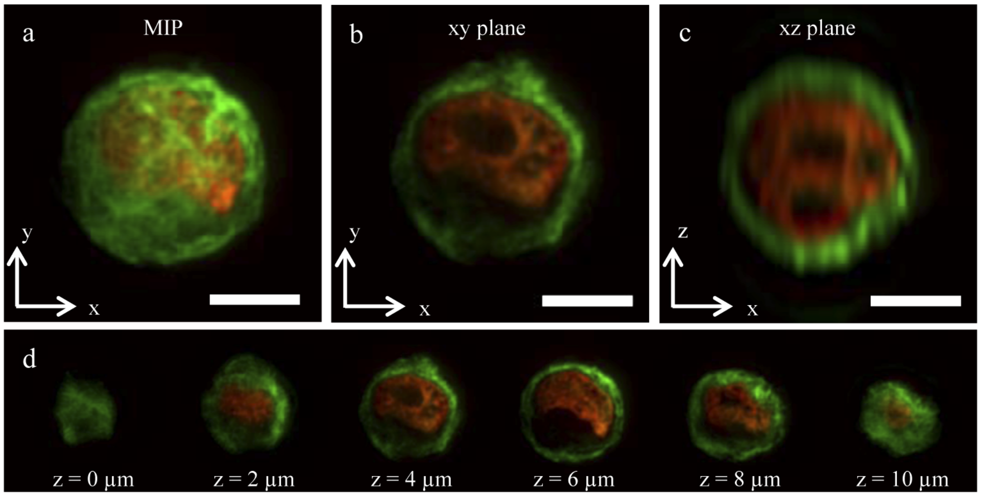

Fig. 5. Double channel single WT IMEC cell acquisition. (a) xy plane Maximum Intensity Projection. (b) Single acquired XY plane. (c) Single reconstructed xz plane. (d) Sequence of xy plane acquisitions at different z during cell passage. Scalebar 5 μm. Alexa488 and mCherry channels represented in green and red respectively.

During the experiment we used a laser power of about 3 mW measured at the device optical fiber input. This low light intensity allows eventually to scan the same cell several times while still maintaining high image contrast, because of the low photobleaching.

A typical acquisition is shown in Fig. 5, where the mCherry and Alexa488 signals are represented with red and green colors respectively. The lateral views consist in around $100 - 200$ slices. We performed deconvolution on the acquired images, with a custom-made software, by minimizing the following functional:

$$\Psi(x) = \|y - Kx\|_2^2 + \mu TV(x) \tag{1}$$

where x is the recovered volume, y is the data volume, K is the convolution kernel, TV is the Total Variation regularisation functional and μ is the hyperparameter setting the weight of the regularisation with respect to the data-fit term. The TV functional is given by:

$$TV(x) = \int |\nabla x|\, dx \tag{2}$$

To minimize Eq. (1) the TwiST algorithm [26] has been used. The optimal hyperparameter μ has been selected with the L-curve method [27]. In the deconvolution we used the experimental lateral PSF (acquired with beads) and an axial PSF corresponding to the experimental light-sheet thickness. A video showing the images stack of Fig. 5 before and after deconvolution is reported in Visualization 2.

The quality of the images allows the clear visualization of features inside the nucleus in the single plane (Fig. 4(b)) and in the different cell sections (Fig. 4(d)). In both xy (Fig. 4(b)) and xz (Fig. 4(c)) views, the nucleoli are visible. On the other hand, the sub-structure of the membrane (e.g. the filament structure of the alpha-tubulin, in green) is more clear in the xy plane than in the xz one. The main reason of the image blur along z direction can be found in the thickness of the light sheet (2.1 μm), while the transverse resolution is limited by the detection objective. Furthermore, the image presents the same quality across the whole xy plane, and this suggests that the light-sheet presents a uniform thickness and illumination and that the sample is sufficiently transparent, avoiding in this way stripe artefacts that are typically present in LSFM images of high scattering samples.

5. Conclusions

In this work we presented an integrated microscope-on-chip for high resolution single-cell LSFM analysis. It is composed by a microchannel and an embedded cylindrical hollow microlens. The channels and the lenses have been designed and optimized to match the small dimensions of the sample, both in terms of handling capability and imaging resolution. The device was realized with FLICE technique, in the same substrate and during a single irradiation step, guaranteeing in this way precise alignment, compactness and robustness. The fabrication process has been carefully characterized and optimized.

We validated the device using xenograft-derived human breast cancer cells and performing dual-color light-sheet fluorescence analysis and 3D reconstruction. We were able to scan through the sample acquiring tens or hundreds of cell's slices. Thanks to the optical sectioning, cellular inter-nuclear corpuscles and membrane protein structure are clearly distinguishable, both in acquired images (xy plane) and axial reconstructions (xz plane). Using this device we could acquire several cells per minute, automatically scanning the samples through the integrated light sheet, without any need to change the sample vial or to realign the optical system between different acquisitions.

Our device is a powerful tool for automatic single-cell analysis. As future perspective, it is possible to further push the throughput by engineering the fluidic system, and to improve the optical performances by shrinking the light sheet thickness.

Funding

European Union under the Horizon 2020 Framework Programme: H2020 Future and Emerging Technologies (801336 - PROCHIP), H2020 Research Infrastructures (654148 -Laserlab Europe).

Disclosures

The authors declare that there are no conflicts of interest related to this article.

References

1. J. Huisken, J. Swoger, F. D. Bene, J. Wittbrodt, and E. H. K. Stelzer, "Optical Sectioning Deep Inside Live Embryos by Selective Plane Illumination Microscopy," Science **305**(5686), 1007–1009 (2004).
2. O. E. Olarte, J. Andilla, E. J. Gualda, and P. Loza-Alvarez, "Light-sheet microscopy: a tutorial," Adv. Opt. Photonics **10**(1), 111 (2018).
3. T. V. Truong, W. Supatto, D. S. Koos, J. M. Choi, and S. E. Fraser, "Deep and fast live imaging with two-photon scanned light-sheet microscopy," Nat. Methods **8**(9), 757–760 (2011).
4. P. J. Keller, A. D. Schmidt, A. Santella, K. Khairy, Z. Bao, J. Wittbrodt, and E. H. K. Stelzer, "Fast, high-contrast imaging of animal development with scanned light sheet-based structured-illumination microscopy," Nat. Methods **7**(8), 637–642 (2010).
5. F. Pampaloni, N. Ansari, and E. H. K. Stelzer, "High-resolution deep imaging of live cellular spheroids with light-sheet-based fluorescence microscopy," Cell Tissue Res. **352**(1), 161–177 (2013).
6. M. Ovečka, L. Vaškebová, G. Komis, I. Luptovčiak, A. Smertenko, and J. Šamaj, "Preparation of plants for developmental and cellular imaging by light-sheet microscopy," Nat. Protoc. **10**(8), 1234–1247 (2015).
7. J. Lin, *Microfluidics for Single-Cell Analysis* (Springer, 2019).
8. N. De Souza and N. Rusk, "Single-cell methods," Nat. Methods **9**(1), 35 (2012).
9. P. Paiè, R. Martínez Vázquez, R. Osellame, F. Bragheri, and A. Bassi, "Microfluidic Based Optical Microscopes on Chip," Cytometry, Part A **93**(10), 987–996 (2018).
10. E. J. Gualda, H. Pereira, G. G. Martins, R. Gardner, and N. Moreno, "Three-dimensional imaging flow cytometry through light-sheet fluorescence microscopy," Cytometry, Part A **91**(2), 144–151 (2017).
11. R. Regmi, K. Mohan, and P. P. Mondal, "High resolution light-sheet based high-throughput imaging cytometry system enables visualization of intra-cellular organelles," AIP Adv. **4**(9), 097125 (2014).
12. J. Wu, J. Li, and R. K. Y. Chan, "A light sheet based high throughput 3D-imaging flow cytometer for phytoplankton analysis," Opt. Express **21**(12), 14474 (2013).
13. E. J. Gualda, H. Pereira, T. Vale, M. F. Estrada, C. Brito, and N. Moreno, "SPIM-fluid: open source light-sheet based platform for high-throughput imaging," Biomed. Opt. Express **6**(11), 4447–4456 (2015).
14. H. Mikami, J. Harmon, H. Kobayashi, S. Hamad, Y. Wang, O. Iwata, K. Suzuki, T. Ito, Y. Aisaka, N. Kutsuna, K. Nagasawa, H. Watarai, Y. Ozeki, and K. Goda, "Ultrafast confocal fluorescence microscopy beyond the fluorescence lifetime limit," Optica **5**(2), 117 (2018).
15. T. A. M. Iura, H. I. M. Ikami, A. K. I. Sozaki, T. A. I. To, Y. A. O. Zeki, K. E. G. Oda, T. Miura, H. Mikami, A. Isozaki, T. Ito, Y. Ozeki, K. Goda, T. A. M. Iura, H. I. M. Ikami, A. K. I. Sozaki, T. A. I. To, Y. A. O. Zeki, and K. E. G. Oda, "On-chip light-sheet fluorescence imaging flow cytometry at a high flow speed of 1 m/s," Biomed. Opt. Express **9**(7), 3424 (2018).
16. M. B. M. Meddens, S. Liu, P. S. Finnegan, T. L. Edwards, C. D. James, and K. A. Lidke, "Single objective light-sheet microscopy for high-speed whole-cell 3D super-resolution," Biomed. Opt. Express **7**(6), 2219 (2016).
17. R. Galland, G. Grenci, A. Aravind, V. Viasnoff, V. Studer, and J. B. Sibarita, "3D high-and super-resolution imaging using single-objective SPIM," Nat. Methods **12**(7), 641–644 (2015).
18. P. Paiè, F. Bragheri, A. Bassi, and R. Osellame, "Selective plane illumination microscopy on a chip," Lab Chip **16**(9), 1556–1560 (2016).
19. R. Osellame, H. J. Hoekstra, G. Cerullo, and M. Pollnau, "Femtosecond laser microstructuring: An enabling tool for optofluidic lab-on-chips," Laser Photonics Rev. **5**(3), 442–463 (2011).
20. K. C. Vishnubhatla, N. Bellini, R. Ramponi, G. Cerullo, and R. Osellame, "Shape control of microchannels fabricated in fused silica by femtosecond laser irradiation and chemical etching," Opt. Express **17**(10), 8685–8695 (2009).
21. E. S. Barnard, "ScopeFoundry,".
22. V. Poli, L. Fagnocchi, A. Fasciani, A. Cherubini, S. Mazzoleni, S. Ferrillo, A. Miluzio, G. Gaudioso, V. Vaira, A. Turdo, M. Gaggianesi, A. Chinnici, E. Lipari, S. Bicciato, S. Bosari, M. Todaro, and A. Zippo, "MYC-driven epigenetic reprogramming favors the onset of tumorigenesis by inducing a stem cell-like state," Nat. Commun. **9**(1), 1024 (2018).
23. M. D. Feit, T. I. Suratwala, L. L. Wong, W. a. Steele, P. E. Miller, and J. D. Bude, "Modeling wet chemical etching of surface flaws on fused silica," Proc. SPIE **7504**, 75040L (2009).
24. P. Paiè, F. Bragheri, T. Claude, and R. Osellame, "Optofluidic light modulator integrated in lab-on-a-chip," Opt. Express **25**(7), 7313 (2017).
25. P. Paiè, F. Bragheri, R. M. Vazquez, and R. Osellame, "Straightforward 3D hydrodynamic focusing in femtosecond laser fabricated microfluidic channels," Lab Chip **14**(11), 1826–1833 (2014).
26. J. M. Bioucas-Dias and M. A. T. Figueiredo, "A new TwIST: Two-step iterative shrinkage/thresholding algorithms for image restoration," IEEE Trans. on Image Process. **16**(12), 2992–3004 (2007).
27. P. C. Hansen, "Analysis of Discrete Ill-Posed Problems by Means of the L-Curve," SIAM Rev. **34**(4), 561–580 (1992).